HYDRO-THERMAL-MECHANICAL COUPLING PROPERTIES AND MESOSCALE SIMULATION OF CONCRETE-ROCK COMPOSITES

GIOVANNI DI LUZIO*, LU FENG†, GIANLUCA CUSATIS‡, KE YU, EROL LALE, AND XUDONG CHEN

* Politecnico di Milano, Department of Civil and Environmental Engineering
Piazza Leonardo da Vinci n.32, 20133 Milan, Italy
e-mail: giovanni.diluzio@polimi.it

†Hohai University, Civil Engineering and Transportation College
Xikang Road n.1, 210024 Nanjing, China
Politecnico di Milano, Department of Civil and Environmental Engineering
Piazza Leonardo da Vinci n.32, 20133 Milan, Italy
e-mail: lufeng980509@hotmail.com

Key words: Fiber Reinforced Concrete, Rock, Composites, Hydro-Thermal-Mechanical Coupling, LDPM Simulation

Abstract. This study examines the essential mechanical and diffusion properties of fiber-reinforced concrete, limestone rock, and their combination with varying interface inclination angles. It focuses on the fracture characteristics, flow behavior, and heat transfer of these composites in the context of hydro-thermal-mechanical (HTM) coupling under triaxial compression. The research is divided into two parts. The first part focuses on studying hydro-thermal-mechanical (HTM) coupling through an extensive experimental investigation. Composite specimens made of fiber-reinforced concrete and limestone rock were fabricated into cylindrical samples with different interface angles of 0°, 15°, 30°, and 45°. Various combinations of hydro-mechanical (HM) tests, thermal-mechanical (TM) tests, and HTM tests were conducted under four different confining pressures (0 MPa, 3 MPa, 6 MPa, and 9 MPa), five water pressures (1 MPa, 2 MPa, 3 MPa, 4 MPa, and 5 MPa), and two temperatures (50°C and 80°C). The results indicated that water pressure slightly weakened the strength of the composite and increased its permeability. Temperature had a significant effect, greatly reducing both the strength and elastic modulus of the composite. Meanwhile, confining pressure enhanced the peak stress and deformation capacity while suppressing permeability. The second part of the study focuses on mesoscopic modeling, which has been calibrated and validated against experimental results. This mesoscale model uses a discrete element method that combines the Lattice Discrete Particle Model (LDPM) with the Flow Lattice Model (FLM). This study simulates the damage characteristics, fluid flow, and heat flux of composites under various combined conditions, including confining pressure, water pressure, and temperature. The results include the stress-strain response, failure modes, cumulative fluid volume, penetration depth, and the non-uniform distribution of heat.

1 INTRODUCTION

Tunnels are frequently exposed to extremely challenging environments characterized by high in-situ stress, elevated temperatures, and the presence of seepage. In response to these conditions, fiber-reinforced concrete (FRC) has emerged as a widely utilized support material due to its unique properties. FRC integrates

with the surrounding rock to form a robust structural layer that provides essential support to the tunnel structure. One of the key advantages of FRC is its excellent ductility, which allows it to deform under stress without fracturing, thus enhancing the overall resilience of the tunnel.

However, the behavior of the concrete-rock composite can be significantly influenced by various external factors found in complex underground settings. These factors include not only the mechanical stresses imposed by the surrounding earth but also thermal variations, which can lead to expansion or contraction, and hydraulic pressures from groundwater or seepage. The interplay of these elements can create a challenging environment for the structural integrity of the composite.

Moreover, the mechanical behavior of FRC-rock composites can differ based on the angle of the interface between the concrete and the rock. Variations in interface inclination can impact the load-bearing capacity of the system and the mechanisms through which water is transported. These factors are crucial in understanding how the composite will perform under varying conditions.

Given these complexities, it is imperative to conduct thorough investigations into the mechanical responses and damage mechanisms of FRC-rock composites, particularly in the context of multi-field coupling effects. Such research is not only vital for enhancing our understanding of material behavior under extreme conditions but also plays a significant role in ensuring the safety and longevity of underground structures. By addressing these challenges, we can develop more effective design strategies and maintenance practices that will ultimately protect these critical infrastructures.

This study performs comprehensive thermo-hydro-mechanical (THM) triaxial compression tests on fiber-reinforced composite (FRC) and rock composites, focusing on how varying interface inclinations affect their behavior. Using an enhanced version of the HTC theoretical model [1, 2], we aim to capture the intricate interactions between thermal conditions, pore pressure, and confining pressure.

Our investigation includes detailed analysis of the mechanical responses of the composites, examining how they deform and fail under different environmental conditions. We also explore the various failure modes and damage mechanisms that arise as a result of these interactions. By conducting numerical simulations alongside our experimental work, we enhance our understanding of the factors influencing the performance and stability of FRC-rock composites in realistic conditions. This research contributes valuable insights into the design and application of these materials in geotechnical engineering and other related fields.

2 MATERIALS AND EXPERIMENTS
2.1 Raw materials and preparation

The specimen is made up of fiber-reinforced concrete (FRC) and limestone rock. The mix ratio of FRC is the same as that of shotcrete in tunnel engineering, and in order to reduce the dispersion of test results, the method of pouring rather than spraying was adopted when preparing samples in the laboratory. Compared to plain concrete, FRC has smaller coarse aggregate particle sizes and a higher sand content. The raw materials used include P.O. 42.5 Portland cement (Type I), river sand with a fineness modulus of 2.3, crushed limestone with a particle size of 5-10 mm, water, a high-efficiency polycarboxylate superplasticizer, and polypropylene fibers. The FRC was cast with a fiber volume fraction of 1.0%, and the proportions of the concrete mixture are listed in Table 1. The limestone is sourced from Shandong Province, China, and primarily consists of calcite, calcium carbonate, and dolomite.

The dimensions of the limestone slab are 450 mm × 350 mm × 50 mm. Initially, the limestone slab is placed in a mold, followed by the casting of concrete on top, ensuring a thickness greater than 50 mm. After standard curing for 28 days, composite samples with dip angles of 0°, 15°, 30°, and 45° are cored from the slabs according to the experimental scheme. As per the specifi-

2

cations set by the International Society for Rock Mechanics (ISRM), the cylindrical specimens for triaxial compression testing have a diameter of 50 mm and a height of 100 mm [3]. To ensure the precision of the test results, the deviation in both height and diameter must be less than 0.01 mm, and the flatness deviation at both end faces should not exceed 0.005 mm. The upper part of the specimen consists of rock, while the lower part is concrete (see Figure 1).

Table 1: Mix proportion of concrete (kg/m^3)

Symbol	Cement	Coarse aggregates	Sand
FRC-1.0	430	694	999
Fibers	Water	Superplasticizer	
9.1	215	1.14	

Figure 1: Composites with various inclinations.

2.2 Test equipment

The MTS 647 Hydraulic Grip apparatus was employed to conduct triaxial compression hydro-mechanical coupling tests on composite specimens with different interface inclinations under varying confining and water pressures (Figure 2). Axial and radial strain are measured using linear variable displacement transducers (LVDTs). The AE instrument utilized in this study is the SAMOSTM AE detection system developed by the American company PAC. Four

AE probes are positioned on the surface of the specimen, each located 15 mm from the ends of the specimen. Figure 2 illustrates the specimen's loading configuration.
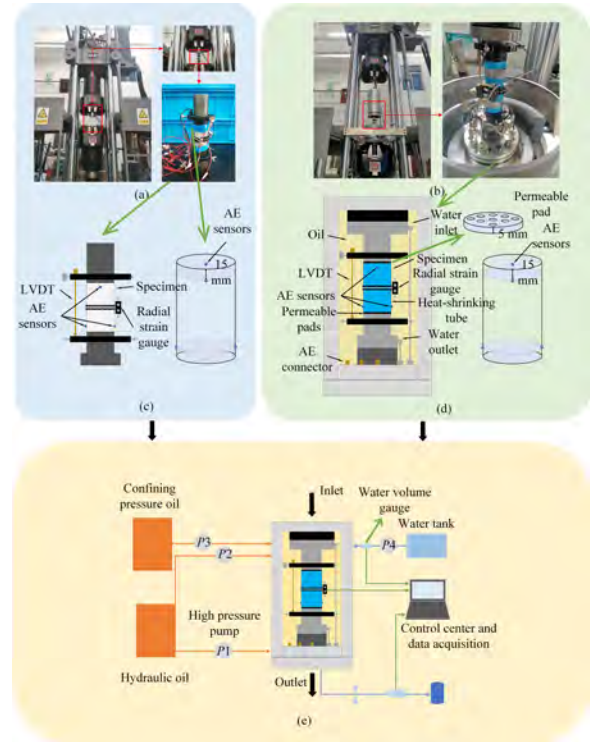

Figure 2: Experiment apparatus.

2.3 Test scheme

2.3.1 Hydro-mechanical coupling

The specimens were initially subjected to vacuum saturation at 100 kPa for 24 hours, and the surfaces were wiped dry before being mounted in the triaxial testing system. Confining pressure was applied to the specimen, and once the predetermined value was reached, water pressure in the axial direction was introduced. Once stable seepage had been established, axial loading was initiated until the specimen failed. The loading was applied by imposing an axial displacement control at a 0.1 mm/min rate. Axial loading continued until the post-peak stage of the specimen, accompanied by AE monitoring. The confining pressure includes 3 MPa, 6 MPa, and 9 MPa, and the water pressure ranges from 1 to 6 MPa.

2.3.2 Thermal-mechanical coupling

Only the thermo-mechanical coupling is considered, so temperature and confining pressure (0 MPa, 6 MPa, and 9 MPa) are set as variables, and saturated samples were used to carry out tests to restore the existence of groundwater. In order to simulate different ground temperature environments, the samples were heated in a water bath. Before the thermo-mechanical coupling triaxial compression tests, the samples were first immersed in a water bath at different temperatures (25°C, 50°C, and 80°C) for 7 days. After the sample was taken out, the test was carried out immediately. When the confining pressure reaches the predetermined value, the axial load is applied in the displacement control mode until the post-peak stage, and the loading rate is 0.1mm /min. In addition, AE monitoring was carried out simultaneously.

Figure 3: Specimens for uniaxial compressive tests.

2.3.3 Thermal-hydro-mechanical coupling

The test temperatures were set at 50°C and 80°C. Samples saturated at these high temperatures were used for thermal-hydro-mechanical coupling tests. During these tests, confining pressures of 3 MPa, 6 MPa, and 9 MPa were applied at a rate of 0.5 MPa/s to a predetermined level, followed by seepage pressures to target values of 2 MPa and 4 MPa. Once the water pressure stabilized, an axial load was applied at a rate of 0.1 mm/min, while acoustic emission (AE) monitoring was conducted simultaneously.

3 EXPERIMENTAL RESULTS

3.1 Uniaxial compressive tests

Uniaxial compression tests were conducted on Fiber-Reinforced Concrete (FRC), limestone, and a composite material using the Wance Universal Testing Machine (Figure 3). The tests were performed on both dry and saturated specimens, which had dimensions of 50 mm in diameter and 100 mm in height, with a loading rate of 0.1 mm/min. The results of the tests are summarized in Table 2. The data indicates that the average strength of limestone is greater than that of the composite material, which, in turn, is stronger than the average strength of FRC. Additionally, the strength of the saturated specimens is observed to be lower than that of the dry specimens.

Table 2: The results of uniaxial compressive tests

Material	State	Average strength
FRC	Natural	41 MPa
FRC	Saturated	37 MPa
Limestone	Natural	54 MPa
Limestone	Saturated	50 MPa
Composite	Natural	54 MPa
Composite	Saturated	39 MPa

3.2 Three-point bending tests

Three-point bending fracture tests were conducted on limestone rock and concrete using the MTS 322 testing machine. The specimens had dimensions of 100 mm × 100 mm × 400 mm and 60 mm × 60 mm × 240 mm. Pre-existing notches, 3 mm in width, were intentionally introduced at the mid-span of each specimen, with a crack-height ratio of 0.4. A COD extensometer was positioned at the bottom of the specimens to measure the Crack Mouth Opening Displacement (CMOD) during the loading process, which occurred at a 0.1 mm/min loading rate.
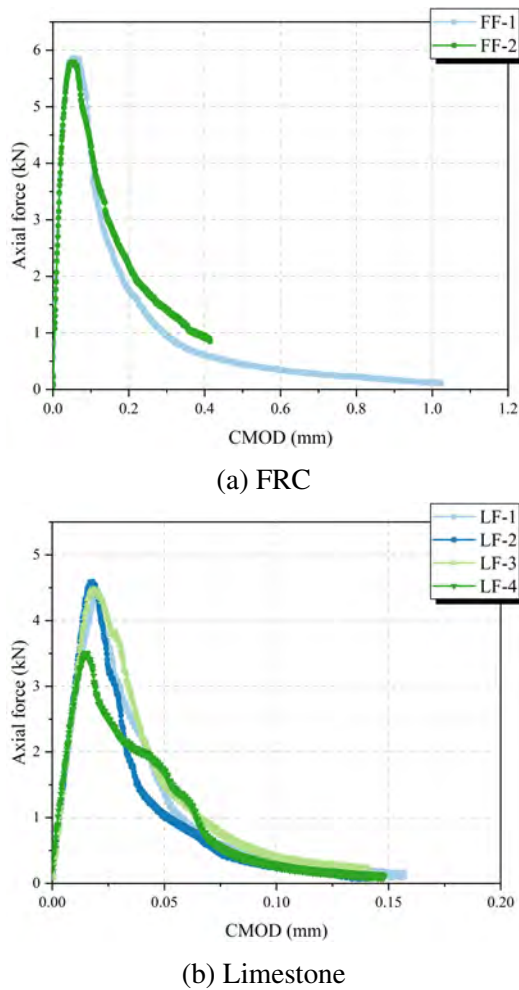
(a) FRC

(b) Limestone

Figure 4: Stress-strain curves for three-point bending tests.

Simultaneously, real-time monitoring of the specimens was conducted using the eight-channel SAMOSTM acoustic emission (AE) detection system developed by PAC, an American company. Figure 4 illustrates the relationship between load and Crack Mouth Opening Displacement (P-CMOD) for the various specimens tested. A clear distinction emerges when comparing the two materials: the CMOD for limestone is considerably lower than that observed in fiber-reinforced concrete (FRC). This significant difference indicates that limestone displays a higher degree of brittleness, leading to less deformation under load. In contrast, FRC showcases enhanced deformation capacity and superior energy dissipation characteristics, suggesting that it can absorb and with-

stand greater stresses without failing. Furthermore, the incorporation of fibers in the concrete mix substantially improves its crack resistance, allowing it to perform more effectively under strain.
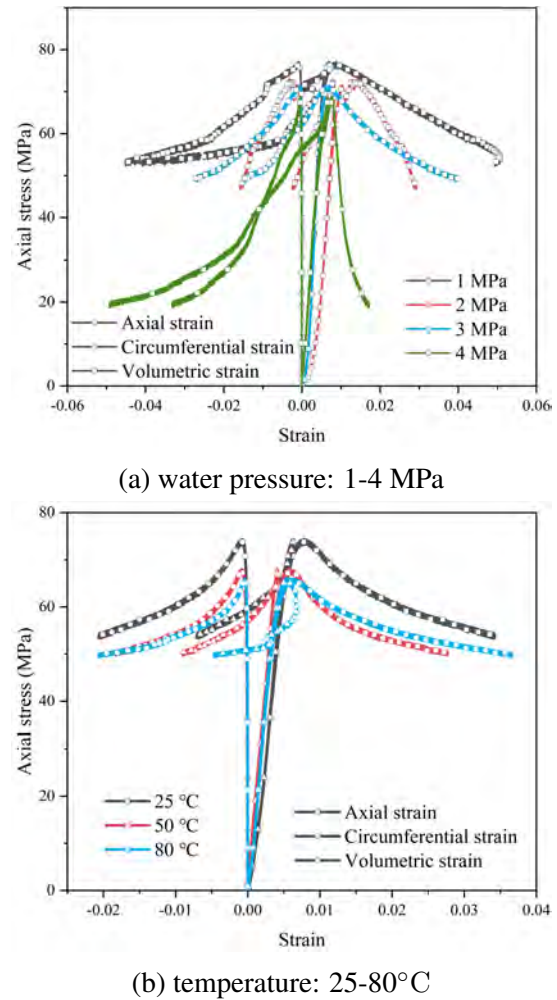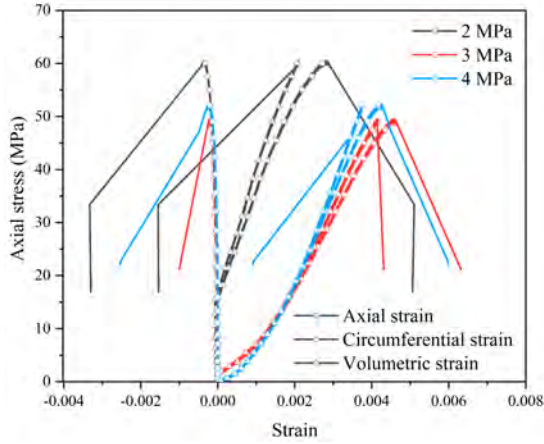

(a) water pressure: 1-4 MPa

(b) temperature: 25-80°C

Figure 5: Stress-strain curve of triaxial compression for composite with 0° interface and confining pressure of 6 MPa.

3.3 Coupling tests

Figures 5 and 6 show the stress-strain curves of FRC/rock composites with different interface inclinations under various coupling conditions. Interface inclination and confining pressure have a significant influence on the mechanical response. The peak stress and strain decrease with the increase of interface inclination. Under the same seepage pressure, with the growth of confining pressure, the peak stress

also increases, exhibiting the confining pressure strengthening effect.

(a) water pressure: 2-4 MPa
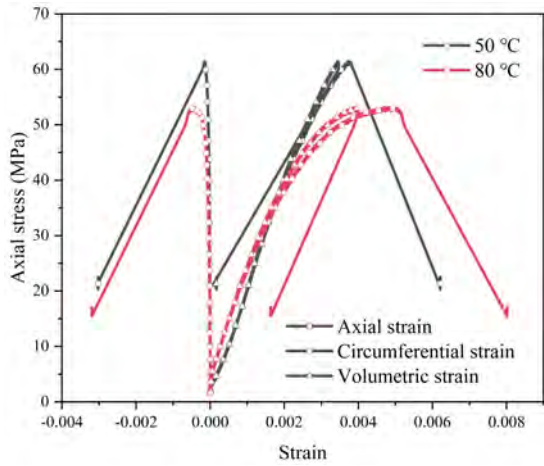
(b) temperature: 25-80°C

Figure 6: Stress-strain curve of triaxial compression for composite with 45° interface and confining pressure of 6 MPa.

Under the same confining pressure, the bearing capacity decreases slightly with the increase of seepage pressure and significantly with the rise of temperature, especially at 80°C. When high temperature and water pressure occur together, confining pressure can help prevent the deterioration of mechanical properties caused by thermal effects. Additionally, as confining pressure increases, the reduction in post-peak softening diminishes, and the material exhibits more pronounced ductile characteristics. For composites with an interface inclined at 45°, the stress decreases sharply after reaching the peak

point, and the post-peak curve does not exhibit any softening behavior.

4 PRELIMINARY NUMERICAL SIMULATION

4.1 Lattice Discrete Particle Model

Cusatis et al. [4, 5] developed a Lattice Discrete Particle Model (LDPM) that effectively simulates the mechanical behavior of quasi-brittle granular materials such as concrete [5], fiber-reinforced concrete [8], and mortar [9].
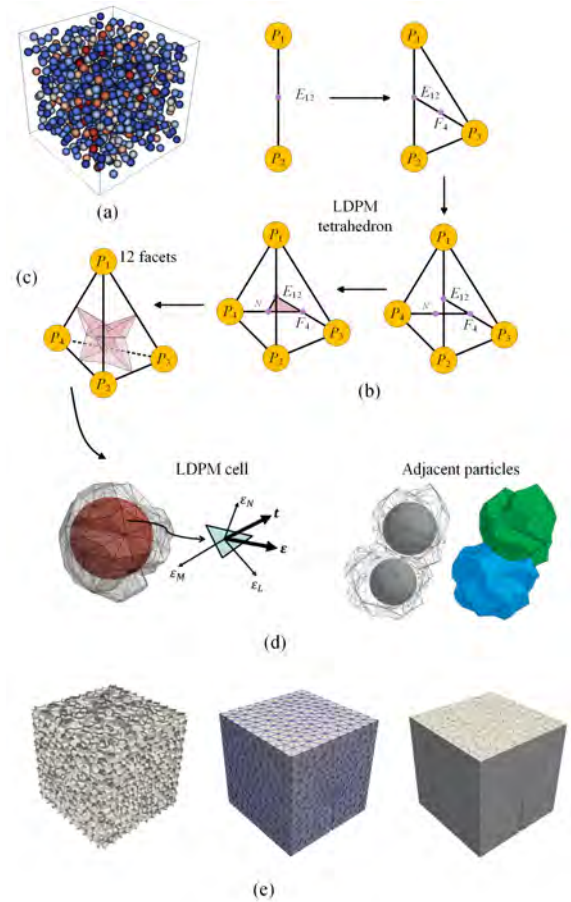

Figure 7: Schematic diagram of LDPM generation principle.

In the model, the cementitious composite is represented as a two-phase system comprising coarse aggregates and the surrounding mortar matrix. A trial-and-error random procedure generates the geometric configuration, where spherical aggregate particles are placed according to a Fuller or Bolomey-type particle size

distribution, Figure 7(a). The Delaunay tetrahedralization of the point system creates a three-dimensional tessellated domain with linear segments connecting particle centers. This results in a lattice of interconnected cells interacting through triangular facets. The mechanical behavior is modeled using four particle subsystems, where nodes (spheres) are linked by edges (struts) with triangular cross sections. The process is shown in Figure 7 (b). The overall deformation of the system is described by rigid body kinematics. Figure 7 (c) shows an LDPM tetrahedron and its 12 facets, which characterize potential failure locations. Figure 7 (e) shows LDPM cells and the model of a volume.

Table 3: Meso-scopic parameters

Symbol	Concrete	Rock
E_0 (MPa)	46,500	139,500
α (-)	0.25	0.25
σ_t (MPa)	5.5	14.8
σ_s (MPa)	11	17
n_t (-)	0.2	0.2
l_t (mm)	150	30
E_d/E_0 (-)	1	1
σ_{c0} (MPa)	100	200
H_{c0}/E_0 (-)	4	4
H_{c1} (-)	0	0
k_{c0} (-)	4	4
k_{c1} (-)	1	1
k_{c2} (-)	5	5
k_{c3} (-)	0.1	0.1
μ_0 (-)	0.5	0.5
μ_∞ (-)	0	0
σ_{N0} (MPa)	400	400

The constitutive model of LDPM consists of two distinct stages: the elastic and the inelastic section. The inelastic behavior includes fractures caused by tensile nominal strain, pore collapse under high compressive hydrostatic pressure, material compaction, and frictional behavior. Additionally, based on the geometry of LDPM, a Flow Lattice Model (FLM) [7] was developed to characterize the diffusion/chemical processes in concrete for various
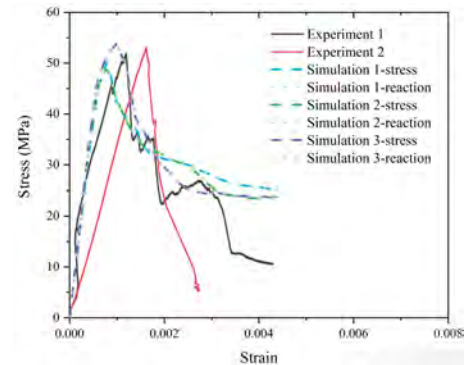
multi-physics applications, such as ASR [11], chloride diffusion [10], and self-healing [12].

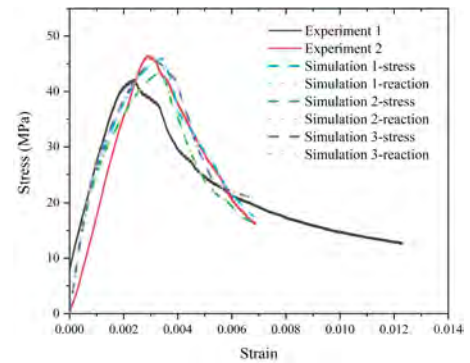## 4.2 Identification of model parameters

Following the calibration of data from uniaxial compression and three-point bending tests conducted on concrete and rock, we successfully derived the mesoscopic parameters of the LDPM for both materials.
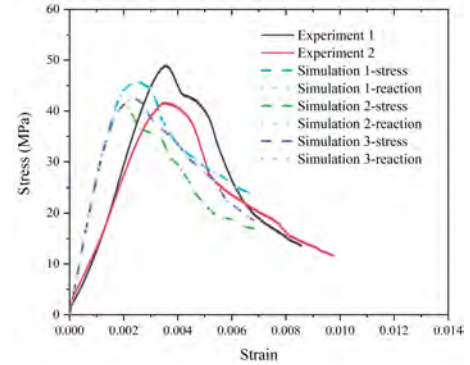
(a) Concrete

(b) Limestone

(c) Composite

Figure 8: Stress-strain curves for uniaxial compression.

These parameters are detailed in Table 3.

7

This analysis provides insights into the mechanical behavior and fracture characteristics of the materials, as presented in the next Section.

4.2.1 Uniaxial compression

Due to the randomness in the aggregate placement of the LDPM, three mesoscopic models were developed for each test, resulting in three separate numerical simulations.

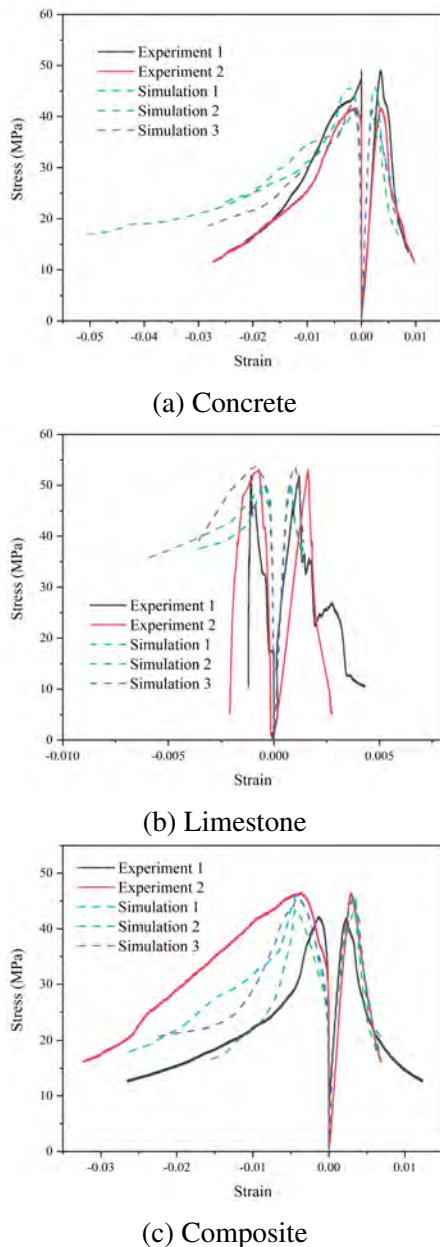(a) Concrete

(b) Limestone

(c) Composite

Figure 9: Axial-circumferential deformation.

Figure 8 illustrates the stress-strain curves of

concrete, rock, and composite materials under uniaxial compression. The simulation results align well with the experimental findings, being the data used to calibrate the model parameters. Figure 9 illustrates the axial and circumferential deformation of concrete, rock, and composite materials. Numerical simulations can effectively reproduce the experimental results, particularly in terms of peak circumferential strain and post-peak behavior. However, due to the brittleness of the rock, sudden fractures occur after reaching peak stress, leading to a rapid drop in stress. This sharp decrease poses challenges when attempting to capture the behavior in numerical simulations.
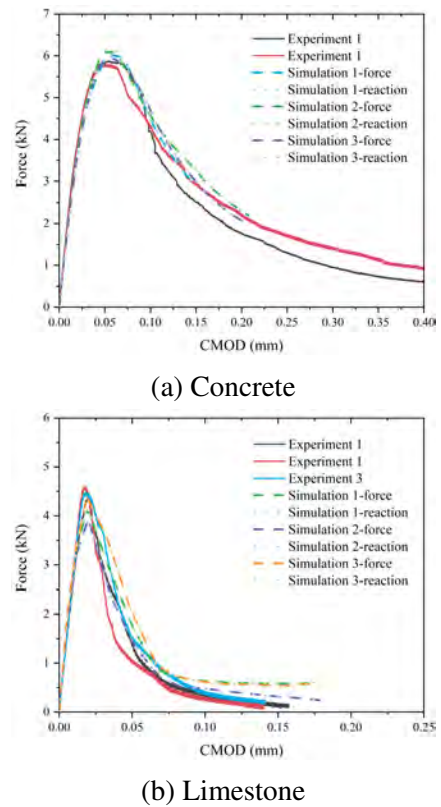

(a) Concrete

(b) Limestone

Figure 10: Force-CMOD curve.

4.2.2 TPB tests

Figure 10 shows a comparison between the TPB simulation results and the test data for both concrete and rock. The numerical simulation results for concrete match perfectly with the test results, as this data was used for calibration.

Additionally, the forces at the two supports at the bottom are approximately equal to the force at the upper loading end, indicating the negligible effect of kinetic forces.

4.2.3 Failure mode

Figure 11 illustrates the failure modes of concrete, rock, and composites under uniaxial compression. materials, which aligns with the experimental results.
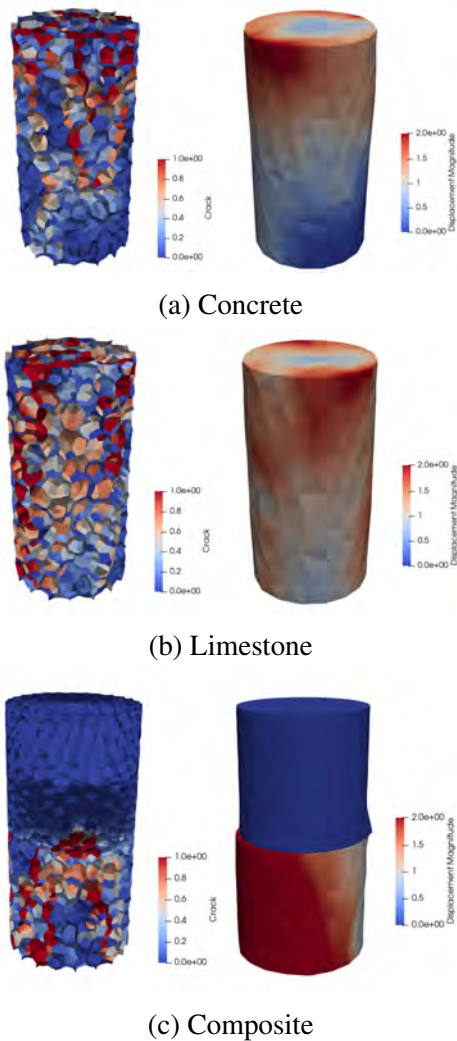

(a) Concrete

(b) Limestone

(c) Composite

Figure 11: Uniaxial compression failure mode.

The locations where cracks propagate are randomly and are predominantly oriented in a vertical direction. The composite has minimal crack development in the rock, and the cracks primarily extend from the interface into the con-

crete at an inclined angle. This indicates that the cracking is mainly due to tensile damage. The expansion of the concrete is more significant than that of the rock, leading to slight relative slipping at the interface between the two Figure 12 illustrates the failure modes of concrete and rock in a three-point bending test. In contrast to uniaxial compression, crack propagation and deformation are more localized. Cracks originate from the notch and extend toward the upper loading end. The deformation of the concrete beam is most pronounced in the mid-span area and near the bottom supports, with the concrete beam experiencing greater deformation than the limestone.
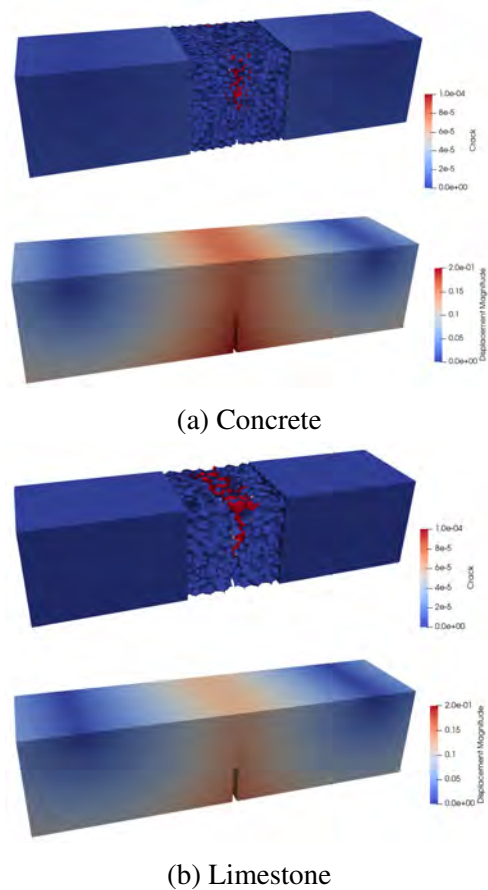

(a) Concrete

(b) Limestone

Figure 12: Three-point bending failure mode.

5 CONCLUSIONS

This paper primarily focuses on conducting basic mechanical tests and multi-field coupling triaxial compression tests on concrete and rock. It also includes the calibration of LDPM meso-

scopic parameters and preliminary numerical simulations based on the experimental results that agree well with the experimental findings. In future work, we plan to conduct numerical simulations of coupling tests based on the multiphysics-lattice discrete particle model.

6 Acknowledgment

REFERENCES

[1] Di Luzio, G., and Cusatis, G. 2009. Hygro-thermo-chemical modeling of high performance concrete. I: Theory. *Cement and Concrete Composites* **31(5)**:301-308.

[2] Di Luzio, G., and Cusatis, G. 2009. Hygro-thermo-chemical modeling of high-performance concrete. II: Numerical implementation, calibration, and validation. *Cement and Concrete Composites* **31(5)**:309-324.

[3] Culshaw, M.G., and Ulusay, R. 2015. The ISRM suggested methods for rock characterization, testing and monitoring: 2007–2014. *Bulletin of Engineering Geology and the Environment* **74(4)**:1499-1500.

[4] Cusatis, G.,Pelessone, D., and Mencarelli, A. 2011. Lattice Discrete Particle Model (LDPM) for failure behavior of concrete. I: Theory. *Cement and Concrete Composites* **33(9)**:881-890.

[5] Cusatis, G., Mencarelli, A., Pelessone, D., and Baylot, J. 2011. Lattice Discrete Particle Model (LDPM) for failure behavior of concrete. II: Calibration and validation. *Cement and Concrete Composites* **33(9)**:891-905.

[6] Li, W., Zhou, X., Carey, J.W., Frash, L.P., and Cusatis, G. 2018. Multiphysics Lattice Discrete Particle Modeling (M-LDPM) for the Simulation of Shale Fracture Permeability. *Rock Mechanics and Rock Engineering* **51(12)**:3963-3981.

[7] Yin, H., Cibelli, A., Brown, S.A., Yang, L.F., Shen, L., Alnaggar, M., Cusatis, G., and Di Luzio, G. 2024. Flow Lattice Model for the simulation of chemistry dependent transport phenomena in cementitious materials. *European Journal of Environmental and Civil Engineering* **28(5)**:1039-1063.

[8] E.A. Schauffert, G. Cusatis, D. Pelessone, J.L. O'Daniel, J.T. Baylot 2012. Lattice Discrete Particle Model for Fiber-Reinforced Concrete. II: Tensile Fracture and Multiaxial Loading Behavior. *Journal of Engineering Mechanics* **138(7)**:834-841.

[9] M Pathirage, F Bousikhane, M D'Ambrosia, M Alnaggar, G Cusatis 2019. Effect of alkali silica reaction on the mechanical properties of aging mortar bars: Experiments and numerical modeling. *International Journal of Damage Mechanics* **28(2)**:291–322.

[10] Y Zhang, G Di Luzio, M Alnaggar, 2021. Coupled multi-physics simulation of chloride diffusion in saturated and unsaturated concrete. *Construction and Building Materials* **292**:123394.

[11] L Yang, M Pathirage, H. Su, M Alnaggar, G Di Luzio, G Cusatis 2021. Computational modeling of temperature and relative humidity effects on concrete expansion due to alkali–silica reaction. *Cement and Concrete Composites* **124**:104237.

[12] A Cibelli, M Pathirage, G Cusatis, L Ferrara, G Di Luzio 2022. A discrete numerical model for the effects of crack healing on the behaviour of ordinary plain concrete: Implementation, calibration, and validation. *Engineering Fracture Mechanics* **263**:108266.